



Seismic attenuation structure of southern Peruvian subduction system

Hyoihn Jang^a, YoungHee Kim^{a,*}, Hobin Lim^a, Robert W. Clayton^b

^a School of Earth and Environment Sciences, Seoul National University, Seoul, 08826, Republic of Korea

^b Seismological Laboratory, California Institute of Technology, Pasadena, CA 91125, United States

ARTICLE INFO

Keywords:

Seismic attenuation
Quality factor (Q)
 t^*
Seismicity
Subduction zone system
Nazca Ridge

ABSTRACT

Seismic attenuation provides key constraints on understanding the structure and dynamics of subduction-zone system. In this study, we provide the first three-dimensional P and S -wave attenuation models beneath the Nazca-South America subduction zone by inverting t^* data from 397 local shallow and intermediate-depth earthquakes. The study area covers the southern part of the Peruvian flat-slab region (11° – 15° S) (where the subducting Nazca Ridge is migrating), and the Central Andean Plateau ($\sim 13^{\circ}$ – 18° S) (associated with the subducting Nazca Plate) and the Brazilian mantle lithosphere. We obtain five major features in our attenuation model with seismicity including (1) well-defined along-strike and along-dip Nazca slab structure in terms of low attenuation, (2) high attenuation associated with the passage of Nazca Ridge and present location of the oceanic ridges, (3) high attenuation in the backarc mantle wedge and continental crust, (4) clear image of Brazilian Shield in terms of low attenuation, underthrusting to the west, and (5) high attenuation related to the slab dehydration beneath the volcanic arc at 100 and 200 km depths. In particular, prominent low- Q zones in the continental crust and mantle wedge beneath the active volcanic arc reflect source zones of arc magmatism caused by fluids from the slab dehydration. The observed along-arc differences in slab Q estimates can be attributed to different hydration states between the flat and normal-dip slabs due to the subduction of the Nazca Ridge.

1. Introduction

The Nazca-South America subduction zone in South America shows significant along-strike variations in seismological properties. Along the South American margin between 10° and 19° S latitude, the Nazca Plate has an age of about 42–52 Ma from northwest to southeast and subducts at average convergence rate of 6.8 cm/yr (Norabuena et al., 1998). This region involves slab-dip variability along the margin (Lim et al., 2018, and references therein). In particular, significant subduction-zone complexities have been attributed to the subduction of the Nazca Ridge which has been migrating southward along the plate margin since ~ 11 Ma (Hampel, 2002), and its present location coincides with the southern end of the flat subduction segment (Hampel, 2002). Several arrays have broadly covered the subduction zone for ~ 1000 km along the arc (Fig. 1). One of the key premises of analyzing such array datasets is to understand how the subducting Nazca slab and/or Nazca Ridge interact with the surrounding mantle and/or continental plate over geological time scales.

Subduction-zone seismic attenuation is a key parameter that helps unravel complex geodynamic processes caused by interaction of subducting Nazca slab and Nazca Ridge with the surrounding mantle and

continental plate. In this study, we provide the first seismic attenuation models based on the regional earthquakes recorded from the several dense seismic arrays (Fig. 1). Based on the models, we first investigate along-strike and along-dip variations in the Nazca plate geometry and seismic attenuation properties, and secondly their relationship to temperature variation beneath the Nazca-South America subduction zone. We further examine correlation between seismic velocity and attenuation structures to gain a better understanding of the physical nature of the attenuation anomalies.

2. Tectonic setting

Along the plate margin between 8° N and 45° S latitude, the Nazca Plate subducts beneath the South American Plate, causing seismicity and upper-plate deformation. In particular, our study region involves the transition in slab geometry from nearly horizontal to normal-dipping from northwest to southeast along the arc (Cahill and Isacks, 1992; Hayes et al., 2012; Phillips et al., 2012; Phillips and Clayton, 2014; Kim and Clayton, 2015; Ma and Clayton, 2015; Lim et al., 2018; Kang and Kim, 2019). Previous studies noted spatial correlation between the flat portion of the subducting Nazca slab and the presence of subducting

* Corresponding author.

E-mail addresses: audtkdrhr@gmail.com (H. Jang), younghkim@snu.ac.kr (Y. Kim), hbim7676@snu.ac.kr (H. Lim), clay@gps.caltech.edu (R.W. Clayton).

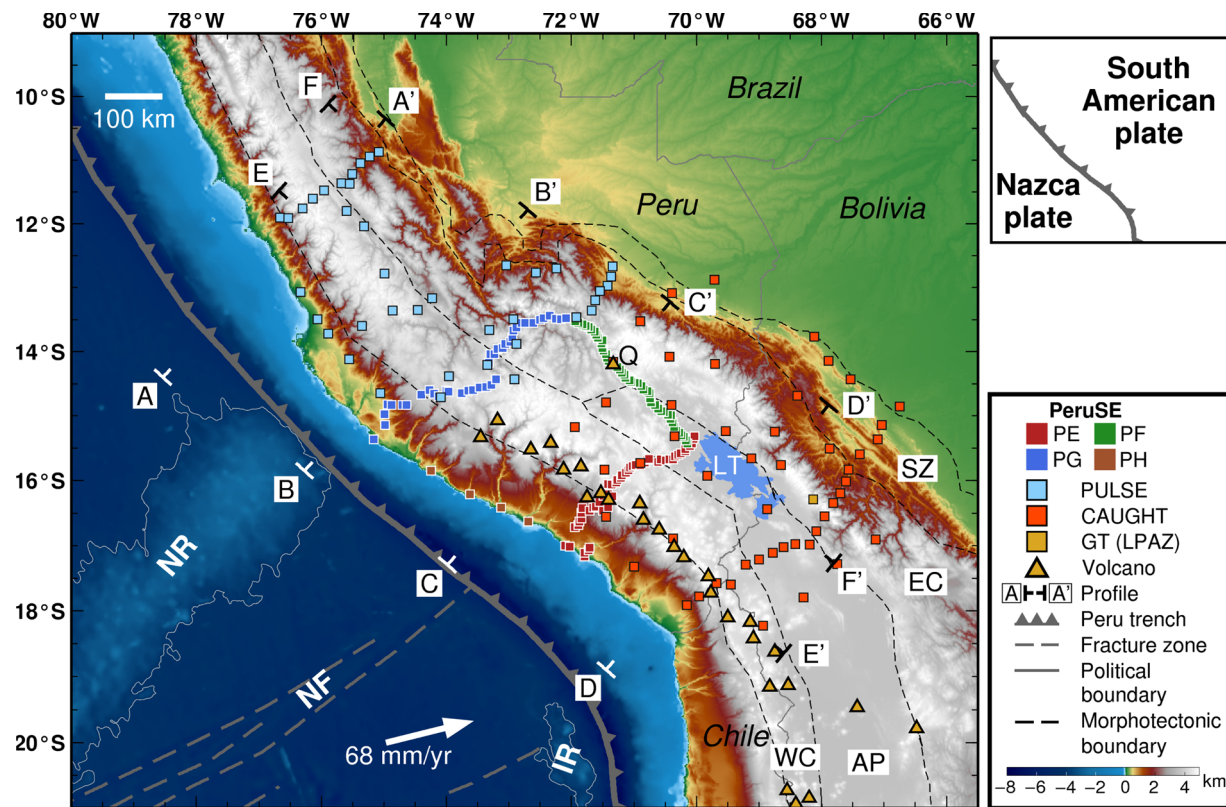


Fig. 1. Study region showing stations (colored squares) that we use to measure t^* . Seismic data used in t^* data analysis are from Peru Subduction Experiment (PeruSE; PeruSE, 2013), Peru Lithosphere and Slab Experiment (PULSE; Wagner et al., 2010), Central Andes Uplift and Geophysics of High Topography experiment (CAUGHT; Beck et al., 2010), and one permanent GT station (LPAZ) (GTSN, 1993). PE and PF lines are part of the PeruSE, sampling normal-dip slab region and along-strike slab-dip transition region in the backarc, respectively. The locations of active volcanoes are shown as yellow triangles, and the location of Quimsachata, in particular, is located in an isolated area far east of the main volcanic front. Profiles A-A', B-B', C-C' and D-D' are set perpendicular to the trench, and profiles E-E' and F-F' are set roughly parallel to the trench. Boundaries of the subducting Nazca Ridge are indicated as thin white lines (Hampel, 2002). Data for fracture zone is taken from Matthews et al. (2011). Data of bathymetry and topography are from Amante and Eakins (2009). Convergence rate between the plates (white arrow) is from Norabuena et al. (1998). See Fig. S1 for the projected location of Nazca Ridge and Nazca fracture zone. WC—Western Cordillera. EC—Eastern Cordillera. AP—Altiplano Plateau. SZ—Subandean Zone. LT—Lake Titicaca. Q—Quimsachata volcano. NR—Nazca Ridge. NF—Nazca fracture zone. IR—Iquique Ridge.

Nazca Ridge (Gutscher et al., 2000). While the cause of the Peruvian flat slab subduction is not clear (Skinner and Clayton, 2013), one possible contributing factor is the subduction of buoyant and hydrated Nazca Ridge (Gutscher et al., 2000; Kim and Clayton, 2015; Ma and Clayton, 2015; Hu and Liu, 2016). Flat slab subduction in South America is of particular interest because it has been associated with tectonic processes such as the cessation of arc volcanism (Ramos and Folguera, 2009), crustal shortening and thickening of the overriding plate, and the evolution of high plateaus (Garzione et al., 2017, and references therein). Also, this region is unusual because the Nazca slab remains nearly flat for ~ 800 km along the arc at ~ 85 km depth, unlike other places like Chile (e.g., Porter et al., 2012) or Mexico (e.g., Kim et al., 2010).

The prominent upper-plate feature in South America is the Central Andean Plateau at $\sim 13\text{--}22^\circ\text{S}$ (Fig. 1), that is associated with abundant arc magmatism, crustal shortening and thickening (Allmendinger et al., 1997). The high plateau of the Central Andes stretches 1800 km along the backbone of the range, from southern Peru to northern Argentina, and varies between 350 and 400 km in width (Allmendinger et al., 1997). The central Andes consists of parallel Eastern Cordillera, an inactive basement-cored fold-and-thrust belt and Western Cordilleras, active magmatic arc, with respect to the Altiplano Plateau in the center (Garzione et al., 2017, and references therein) (Fig. 1). The thin-skinned Subandean fold and thrust belt in the eastern part of Eastern Cordillera constitutes the easternmost part of the Andean orogen that reflects shortening and eastward propagation of the Andean deformation front (Garzione et al., 2017, and references therein). The present-

day geodetic measurements suggest shortening rates no higher than 10 mm/yr (Bevis et al., 2001).

3. Data analysis

We divide our study region into four parts with respect to the subducted Nazca Ridge axis in a trench-parallel direction: (1) the region north of the ridge axis, (2) the region of flat-slab subduction, where the Nazca Ridge subducts, (3) the slab-dip transition zone, south of the ridge axis, and (4) the normal-dip subduction zone (Fig. 1). Also, the study region can be subdivided into the four structural units in a trench-perpendicular direction: (1) the forearc, (2) the Western Cordillera, (3) the Eastern Cordillera, and (4) the Subandean zone (Fig. 1).

We use regional earthquakes in 2008–2013 (Fig. 2a), recorded from one permanent GSN station (LPAZ) and three temporary broadband seismic networks (Fig. 1), which are the Peru Subduction Experiment (PeruSE; PeruSE, 2013), Peru Lithosphere and Slab Experiment (PULSE; Wagner et al., 2010), and Central Andes Uplift and Geophysics of High Topography experiment (CAUGHT; Beck et al., 2010). In particular, the PULSE array covers the region north of the ridge axis (north of 14°S), where the Nazca Ridge has passed through (Fig. 1). The PeruSE, consisting of three dense seismic array lines surrounding the region between the flat slab system (near the ridge axis) and normal-dip slab systems and four stations deployed along the coast (Fig. 1), covers the slab-dip transition zone. The slab-dip transition zone is defined as a region between the southern edge of the flat slab segment ($\sim 14^\circ\text{S}$) and the normal-dip ($\sim 30^\circ$) slab region (Lim et al., 2018). The CAUGHT

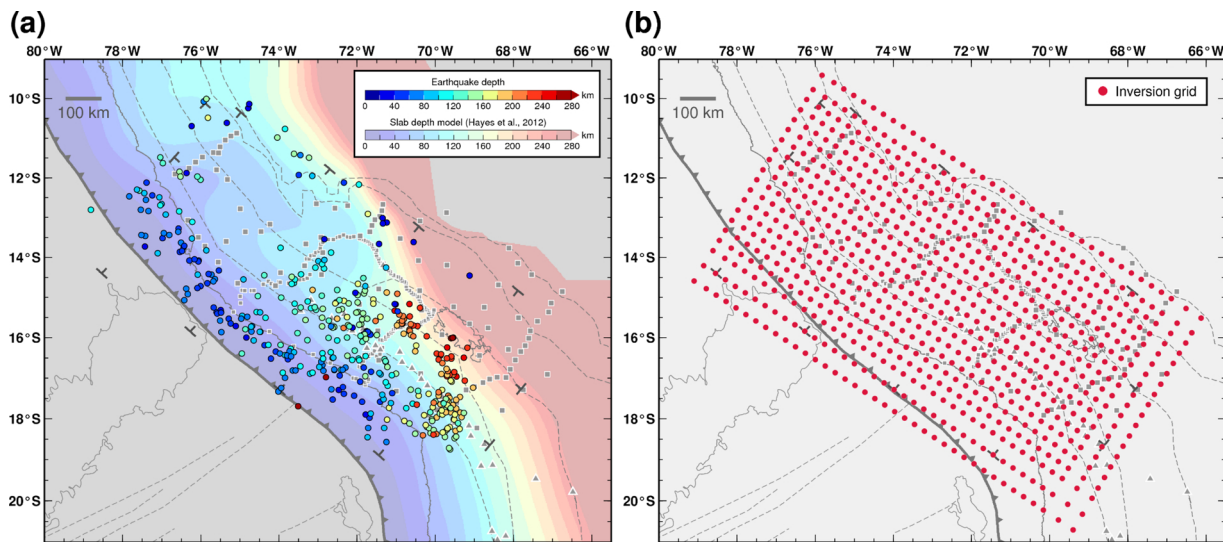


Fig. 2. Earthquake locations and inversion grid. (a) Total 397 relocated hypocenters used for the inversion. Background colors represent slab geometry from the slab depth model (Slab 1.0) by Hayes et al. (2012). (b) Inversion grid setup. See Fig. 1 for lines and symbols.

covers the region beyond the slab-dip transition zone extending to northwestern Bolivia, and Inquique Ridge is present offshore (Fig. 1).

3.1. Earthquake relocation

We collect earthquakes in catalogues provided by US National Earthquake Information Center (NEIC) and Bulletin of the International Seismological Centre (ISC) that occurred within the distance of 2° from the station network during 2008–2013. The earthquake magnitudes are restricted to 4.0–6.5, and their focal depths range from 20 to 300 km. We determine hypocenters of the earthquakes using a program HYPO-ELLIPE (Lahr, 1989) and a 1D velocity model (Dougherty and Clayton, 2015). The program is based on a linearized iterative method for earthquake locations, which minimizes travel-time residuals between the theoretical prediction and observation. We perform 1000 bootstrapping inversions for determining the earthquake locations. After removing intermediate-depth earthquakes that show scattered guided waves (see Section 3.2 for detail), we select 397 earthquakes for the inversion (Fig. 2a).

3.2. Removal of scattered guided waves

Scattered guided waves are reflected multiples that travel in layers separated from the surrounding medium by high impedance contrasts, and have been observed in various subduction zones (Abers and Sarker, 1996; Martin and Rietbrock, 2006). Slow layers at the top of subducting slabs promote the entrapment of seismic energy, potentially resulting in guided waves with high amplitudes and low-frequency onsets. Previous studies identified the presence of a thin ultra-slow velocity layer atop the subducting plate in southern Peru (Dougherty and Clayton, 2015; Kim and Clayton, 2015). In particular, guided-wave dispersion was observed from earthquakes at 180–280 km depth recorded at stations in the forearc of N. Chile, south of our study region (Garth and Rietbrock, 2017, and references therein). Given the detailed plate geometries constrained from our relocated seismicity and teleseismic receiver functions (Phillips et al., 2012; Phillips and Clayton, 2014; Kim and Clayton, 2015; Ma and Clayton, 2015; Kang and Kim, 2019), we first identify potential earthquakes that occur close to the slab surface and show a slab-guided wave with a small-amplitude low-frequency precursor following large-amplitude high-frequency signals. We then exclude waveforms that include the guided wave arrivals in the attenuation measurement.

4. Methods

Seismic waves lose their energy during their passage through underground materials due to scattering and intrinsic attenuation. The intrinsic attenuation is generally controlled by temperature, composition, melt content, and volatile content of the rocks through which the seismic waves travel. Seismic attenuation is quantified as a quality factor Q , which represents the ratio of energy lost during one cycle to total wave energy. In particular, Q^{-1} is proportional to the grain size, enclosed melt/H₂O content ratio, and temperature (Faul et al., 2004; Aizawa et al., 2008). Since Q is sensitive to temperature variations, seismic attenuation provides meaningful constraints on physical parameters for several key subduction components. Such components are subducting slab, mantle layer between the continental crust and the slab (i.e., mantle wedge), overriding plate, and magma chamber below the volcanic arc.

4.1. Measuring t^* value

The Q is a frequency dependent value that is commonly expressed as

$$Q = Q_0 f^{-\alpha} \quad (1)$$

where α is constant and Q_0 a quality factor when frequency is 1.0 Hz. Here, α is fixed as 0.27 following previous studies for other subduction zones (Stachnik et al., 2004; Rychert et al., 2008). We solve for path-averaged attenuation at 1 Hz (Stachnik et al., 2004; Rychert et al., 2008), and for simplicity, we denote Q_0 as Q . The Q averaged along the raypath is denoted as t^* , which can be expressed as

$$t^* = \int_{\text{raypath}} \frac{dr}{Q(r)V(r)} \quad (2)$$

where V denotes velocity (e.g., Haberland and Rietbrock, 2004).

We set the frequency range as 0.5–20.0 Hz for the spectral analysis, and select a time window of 2.56 s after each P and S phase arrivals, following the data processing scheme outlined by Stachnik et al. (2004) and Chen and Clayton (2009). We set the signal-to-noise ratio (SNR) as 2.0 for P and 1.5 for S , and every arrival time is manually picked and the quality of the waveforms is visually inspected. From the 397 events, we obtain 25,894 t_P^* and 18,143 t_S^* for P and S waves, respectively. We then apply the multi-taper method (Prieto et al., 2009) to convert the time-domain to frequency-domain signals. Examples of waveforms and fittings to the spectra are shown in Fig. 3.

We estimate seismic attenuation from the spectra of the velocity

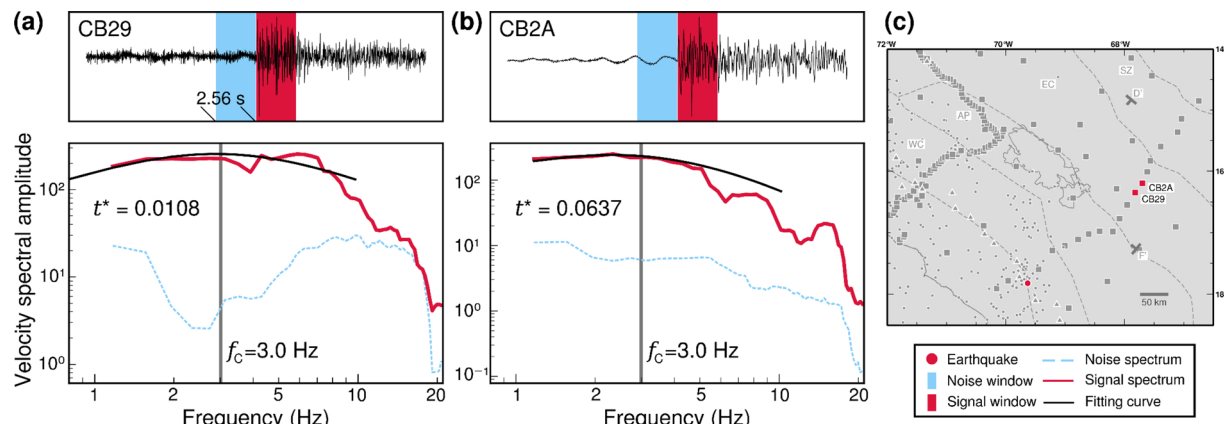


Fig. 3. Example showing P waveforms and t^* fit for one earthquake. Spectrum and waveform of the station (a) CB29 and (b) CB2A. Their station locations are shown in (c). Origin time and depth of the earthquake is 2012/01/11 20:24:19.3 (in format of Y/M/D H:M:S) and 159 km, respectively. A common corner frequency f_c for the earthquake and different t^* for each record are estimated. See Fig. 1 for lines and symbols in (c).

waveforms. The amplitude of the velocity spectrum of i th station for the j th event is

$$A_{ij}(f) = C \times S_j(f) \times B_{ij}(f) \times I_i(f) \quad (3)$$

where f is the frequency, C constant, $S_j(f)$ the source spectrum, $B_{ij}(f)$ the attenuation along the raypath from the event j to station i , and $I_i(f)$ the instrument response (e.g., Anderson and Hough, 1984). We assume ω^{-2} type source model (Brune, 1970) for the source term $S_j(f)$, which can be expressed as

$$S_j(f) = \frac{fM_0}{1 + (f/f_c)^2} \quad (4)$$

where M_0 is the seismic moment and f_c the corner frequency. The attenuation term $B_{ij}(f)$ is expressed as

$$B_{ij}(f) = \exp(-\pi f t_{ij}^*) \quad (5)$$

where t_{ij}^* is the whole-path attenuation operator along the raypath from the event j to station i . We neglect the instrument response term $I_i(f)$ considering our selected frequency range (Chen and Clayton, 2009). The Eq. (3) is now rewritten as

$$A_{ij}(f) = \frac{C'f}{1 + (f/f_c)^2} \exp(-\pi f t_{ij}^*) \quad (6)$$

where C' is constant. We measure t_{ij}^* in the Eq. (6) by fitting the observed velocity spectrum of the raypath. We apply more than 10 iterations to determine a stable t^* as suggested by Eberhart-Phillips and Chadwick (2002). We discard unrealistic t^* values that are not positive or too large. Those values generally result from trapped waves, hence do not represent attenuation estimates.

The corner frequency trades off with t^* (Ko et al., 2012). Following the method by Stachnik et al. (2004), we determine one corner frequency for each event by grid search method. We stack all waveforms for one event and obtain the corner frequency of that event using fixed t^* . According to the formulation by Kanamori and Anderson (1975), the relationship between corner frequency and seismic moment is as follows:

$$f_c = 0.42v_s \left(\frac{\Delta\sigma}{M_0} \right)^{1/3} \quad (7)$$

where v_s represents the near-source velocity, M_0 the seismic moment, and $\Delta\sigma$ the constant stress drop. We retrieve the best estimate for the stress drop by the least square fit to the corner frequency versus seismic moment. The difference between the reference stress drop and calculated value may arise from the difference in focal depth. We thus compare P -wave and S -wave corner frequencies and confirm that they

are roughly in a linear relationship. We then also confirm stability of t^* through a cluster-event analysis (Ko et al., 2012). As a test of the stability of t^* estimates, we use 13 events that occurred in nearly identical locations but with different magnitudes on 15 August 2014. We find that our t^* values for these events are consistent.

4.2. Tomographic inversion

We invert the t^* measurements for 3D Q structure. Travel times are computed with rays traced in the 3D velocity model using a ray tracing algorithm by Um and Thurber (1987) and Zhao et al. (1992). The 3D model includes four-layer structures with interfaces such as a mid-crust, continental Moho, oceanic Moho, and slab surface (Fig. S2). Geometry of the continental Moho and the slab surface are implemented from the Crust 2.0 model (Laske et al., 2013) and Slab 1.0 model (Hayes et al., 2012). We set the mid-crustal interface at 40 km following the receiver function results (Phillips et al., 2012), and the oceanic Moho 10 km below the slab surface. The initial attenuation model has a constant Q^{-1} of 1/200, and each iteration is set to minimize the residuals of most t^* . We solve Q for each grid node in an iterative procedure based on projected Levenberg-Marquardt method (Kanzow et al., 2004).

The source-receiver geometry provides highly uneven ray coverage in our study region. Thus, we take trial and error approach in the checkerboard resolution test to determine optimal grid size for the inversion. To effectively cover our study region, we set slightly larger grid along the edge (0.3°) and smaller grid (0.2°) inside (Fig. 2b). We also let the grid size change with depth (15 km down to a depth of 240 km and 20 km for the larger depth), reflecting the diminishing resolution with depth.

In the inversion procedure, we impose Tikhonov regularization by setting the Tikhonov matrix to an identity matrix (Hansen, 2000) to prevent overfitting. For the regularization, we use L-curve test to determine a damping factor, η . The L-curve test is a log-log plot of the norm of the regularized solution versus corresponding residual norm. For strictly locating the corner of the L-curve, we use a point with the maximum curvature of the curve (Hansen, 2000). In 100 iterations, we determine new η using the L-curve test.

5. Results

5.1. Checkerboard test results

We assess the ability of tomographic inversion as well as the quality of the model given the ray coverage by performing checkerboard sensitivity tests (Figs. 4 and S3). Checkerboard model is created by assigning high and low Q values within the model domain, and in our

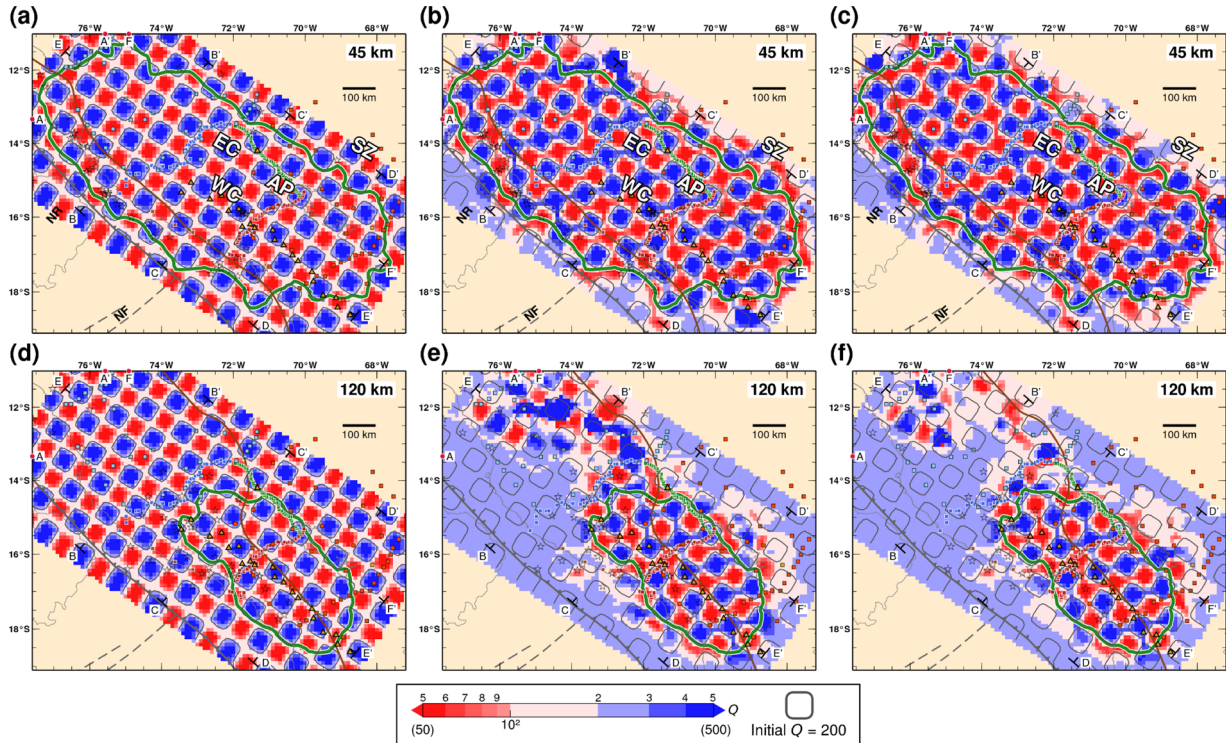


Fig. 4. Horizontal checkerboard test results for Q_p and Q_s at depths of (a–c) 45 km and (d–f) 120 km. Initial Q_p and Q_s structures ranging from 50 to 500 are shown in (a) and (d). Recovered Q_p values are shown in (b) and (e) and Q_s in (c) and (f). Note that the initial Q_p and Q_s for the inversions are set as 200. See Fig. 1 for symbols and Fig. S2 for the results at depths of 75, 90, and 150 km. NR—Nazca Ridge. NF—Nazca fracture zone. WC—Western Cordillera. EC—Eastern Cordillera. AP—Altiplano Plateau. SZ—Subandean Zone.

study, we set Q value of 50 and 500 for the high and low values, respectively. We assign each block size to be bigger than the actual block size by a factor of roughly two for the real data only for display purposes (Figs. 4 and S3).

Using the perturbed model, we calculate t^* at all the data points, and these t^* become input data for the resolution test. The quality of the inversion is directly proportional to ray path coverage, and thus the locations of earthquakes are one of the important factors which controls the resolution at deeper depth. We mask regions, which are not constrained by the data, and such regions are determined by the following criterion:

$$\left| \frac{Q_{\text{recovered}} - Q_{\text{initial}}}{Q_{\text{initial}}} \right| > 0.15 \quad (8)$$

The checkerboard pattern is recoverable in the depth range of 0–225 km. The model resolution for the depth less than 30 km is strongly restricted to regions closest to the stations. The resolution for the deeper depth extent (> 120 km) greatly depends on the location of deep earthquakes and station network geometry. The location of deep events mostly occurs in the eastern side of our study region (Fig. 2a). Overall, the recovered values are slightly overestimated, but are in the reliable error range (< 15%).

The checkerboard test results for both Q_p and Q_s structures ensure the highest resolution in the slab-dip transition zone between flat and normal slab subduction down to a depth of 90 km (Figs. 4 and S3). At the depth greater than 90 km, the resolution becomes poor at the region at/near the subducting the Nazca Ridge and north of the ridge axis due to the relatively smaller number of earthquakes (Figs. 4 and S3). The resolution is sufficiently good at the depth range of 120–150 km to allow examining the slab-dip variation along the trench from the coast to inland covering the backarc system (Figs. 4 and S3).

The Q_s estimates show a similar pattern to that of the Q_p estimates (Figs. 4 and S3); however, they show reduced spatial resolution

primarily due to the lower number of S-wave phase picks. Regardless, we note that the resolution for Q_p and Q_s is sufficient in the region that covers continental crust (from 30 km depth), subducting slab, and mantle layer above the slab. The resolution becomes somewhat limited beyond 150 km, primarily because of the lack of seismicity at deeper depths.

5.2. Q_p and Q_s structures

The inversion results of Q_p and Q_s are presented at the horizontal slice views (Figs. 5, 6, S4, and S5) and vertical cross-sectional views (Figs. 7 and 8). Horizontal depth slices of the tomographic images are useful to examine spatial variation in high and low attenuation anomalies at different depths (0–225 km) (Figs. 5, 6, S4, and S5). On the other hand, the images along the trench-perpendicular profiles A–A', B–B', C–C' and D–D' are useful to examine subduction-zone components such as the subducting Nazca slab, continental crust and mantle wedge in along-strike direction at four different regions (Figs. 7a–d and 8a–d). The images along the trench-parallel profiles E–E' and F–F' are useful to examine the components in along-arc direction (Figs. 7e, f, 8e, and f). In particular, the profile E–E' crosses the volcanic arc front (Fig. 1).

We obtain minor differences between Q_p and Q_s models, and the differences are mostly in the region near the coast where the ray coverage is slightly poor (Figs. 5, 6, S4, and S5). The top slab interface (Slab 1.0; Hayes et al., 2012) and the base of continental crust (Crust 2.0; Laske et al., 2013) are included in the displays for reference.

5.2.1. Nazca slab structure

Our results show notably high Q (both Q_p and Q_s) for the subducting Nazca slab. Both Q_p and Q_s for the slab overall show values of 5×10^2 – 1×10^5 (Figs. 5–8, S4, and S5). In particular, the horizontal slices show the more obvious slab feature characterized by high Q_p and

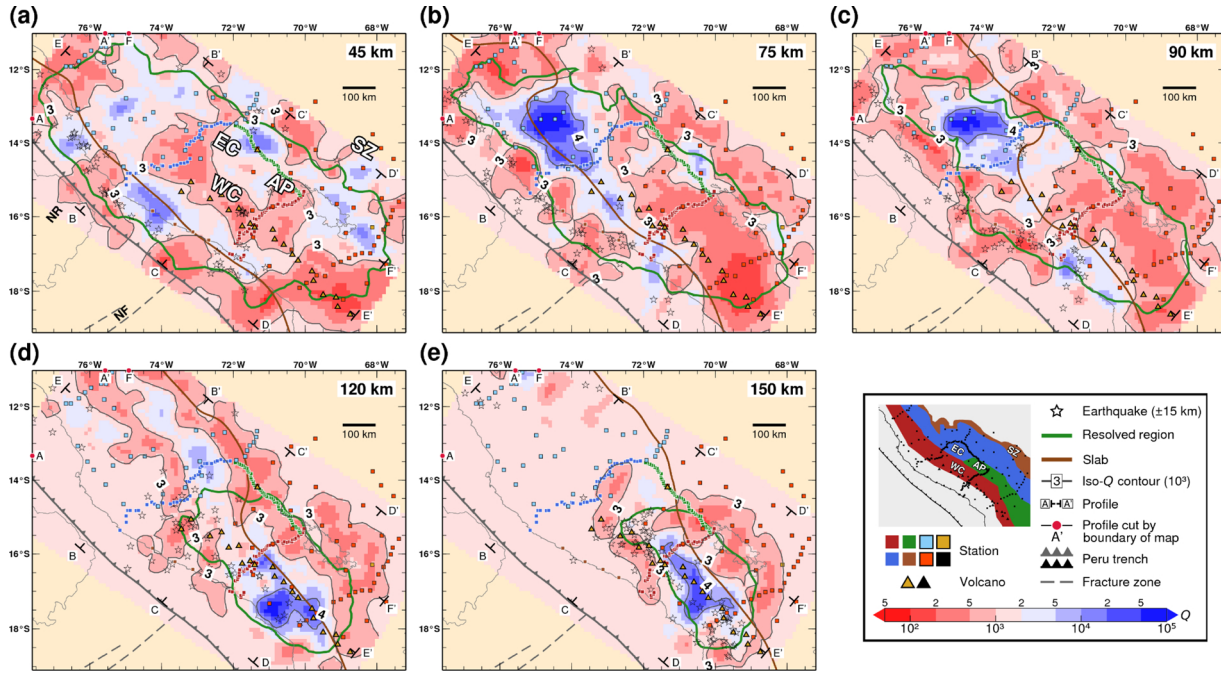


Fig. 5. Horizontal slices of Q_p at depths of (a) 45 km, (b) 75 km, (c) 90 km, (d) 120 km, and (e) 150 km. The depth of the horizontal slice is indicated at upper right corner of each subfigure. See Fig. S4 for Q_p at every slice at 0–280 km depth with 15 km interval depth. NR—Nazca Ridge. NF—Nazca fracture zone. WC—Western Cordillera. EC—Eastern Cordillera. AP—Altiplano Plateau. SZ—Subandean Zone.

Q_s from the top slab interface down to 225 km depth (Figs. 5, 6, S4, and S5). The depth of flattening and inboard extent of the horizontal Nazca slab segment are ~ 80 km and ~ 400 km from the trench, respectively (Figs. 7b and 8b).

Slightly lower Q estimates below the slab surface are found near the coast for the profiles A–A', B–B', and D–D' (Figs. 7a, b, d, 8a, b, and d), and the origin of such anomalies likely varies for different localities. In particular, the subducting slab present north of the ridge axis dominantly shows lower Q estimates along the profile A–A' (Figs. 7a and

8a). This observed low Q_p and Q_s extend at least 200 km from the trench (Figs. 7a and 8a). Also, the low Q anomaly is clearly observed in close proximity to current positions of both Nazca and Iquique ridges along the profiles B–B' (Figs. 7b and 8b) and C–C', respectively (Figs. 7c and 8c).

5.2.2. Continental crust

The continental crust is imaged with generally low Q (both Q_p and Q_s) except the forearc crust, which is shown in relatively high Q (Figs. 7

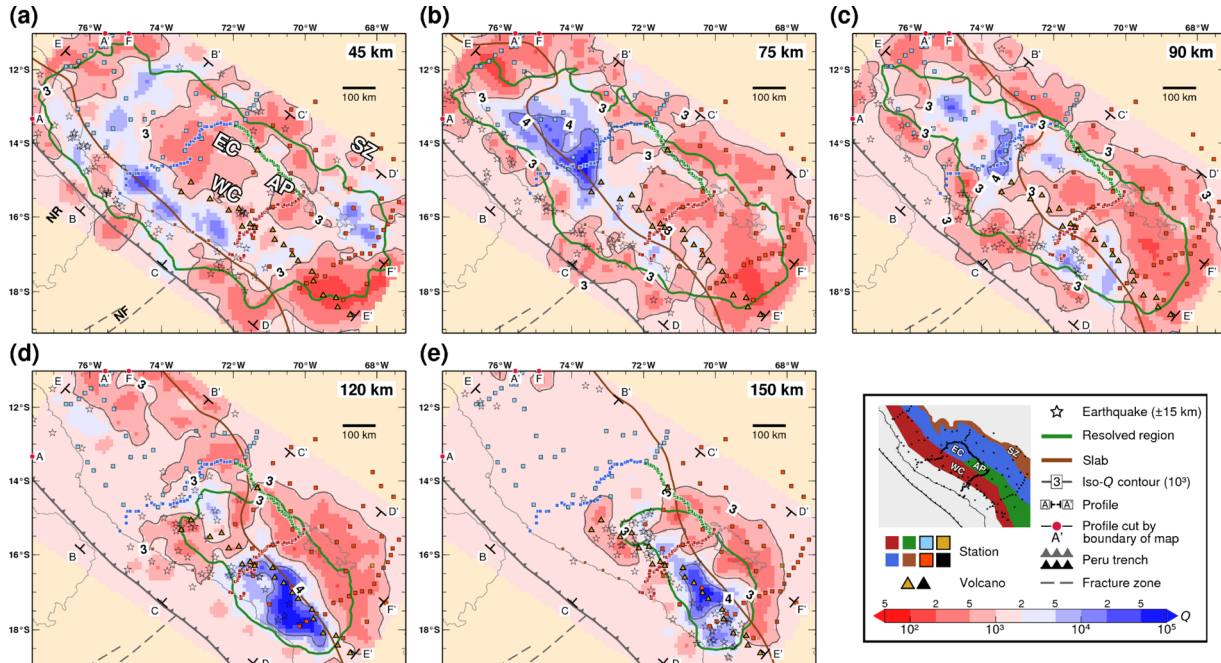


Fig. 6. Horizontal slices of Q_s at depths of (a) 45 km, (b) 75 km, (c) 90 km, (d) 120 km, and (e) 150 km. The depth of the horizontal slice is indicated at upper right corner of each subfigure. See Fig. S5 for Q_s at every slice at 0–280 km depth with 15 km interval depth. NR—Nazca Ridge. NF—Nazca fracture zone. WC—Western Cordillera. EC—Eastern Cordillera. AP—Altiplano Plateau. SZ—Subandean Zone.

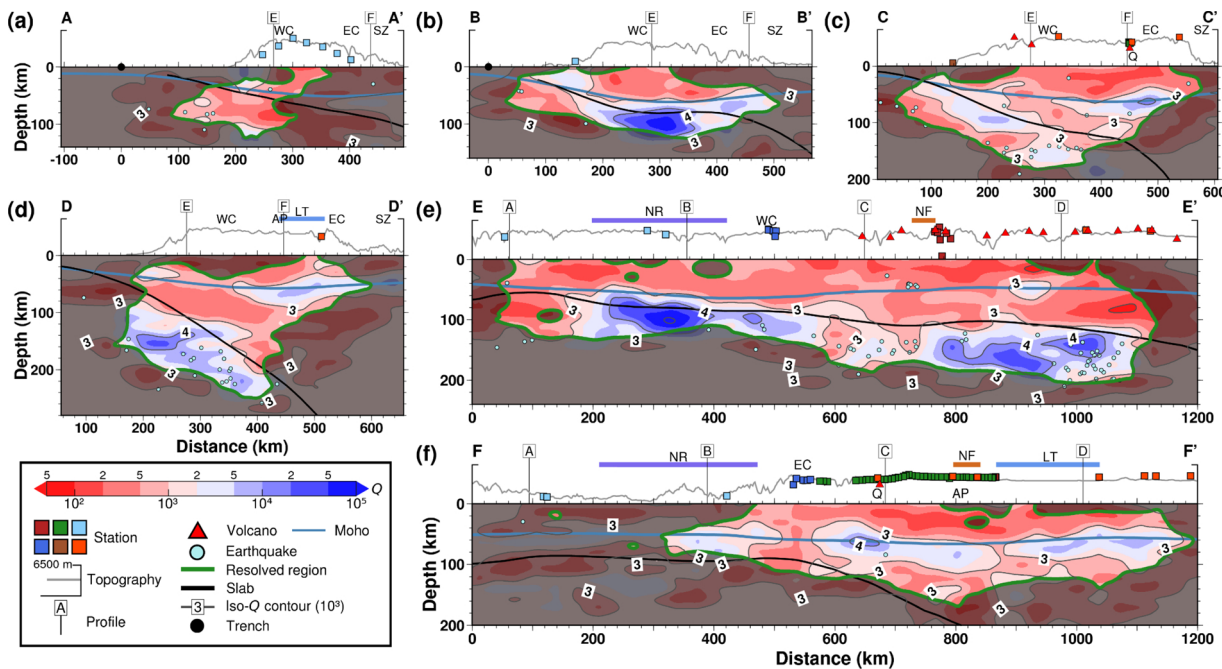


Fig. 7. Q_p in cross-section view along trench-perpendicular profiles (a) A–A', (b) B–B', (c) C–C' and (d) D–D' and trench-parallel profiles (e) E–E' and (f) F–F' for which the locations are indicated in Fig. 1. Lengths of the profiles in (a–d) and (e–f) are 600 km and 1200 km, respectively. The position of 0 km point in the trench-perpendicular profiles (a–d) marks the trench location. Contour level for Q_p is labeled by exponent. The locations for Nazca Ridge (NR), Nazca fracture zone (NF) and Lake Titicaca (LT) are highlighted in the trench-parallel profiles (e and f) (see Fig. S1 for the projected locations of NR and NF). Colored dots indicate relocated seismicity. The top plate interface is retrieved from Slab 1.0 model (Hayes et al., 2012) and Moho from Crust 2.0 model (Laske et al., 2013). WC—Western Cordillera. EC—Eastern Cordillera. AP—Altiplano Plateau. SZ—Subandean Zone. LT—Lake Titicaca. Q—Quimsachata volcano.

and 8). The contrast in Q values across the base of the continental crust broadly agrees with the Moho depth estimates (Crust 2.0; Laske et al., 2013) (Figs. 7 and 8). In general, our models show a thick, 65–75 km crust underneath the Western Cordillera and Altiplano (Figs. 7 and 8). The feature of the thinned crust (~40 km) beneath the Subandean zone

(Ryan et al., 2016) is not clear in our models due to limited resolution (Figs. 7 and 8). In particular, Q_s along the profile F–F' shows a sharp contrast in attenuation across the Moho (Fig. 8f).

We observe low Q_p and Q_s below the volcanic arc along the profiles C–C', D–D', and E–E' (7c–e and 8c–e). In particular, low Q_p and Q_s

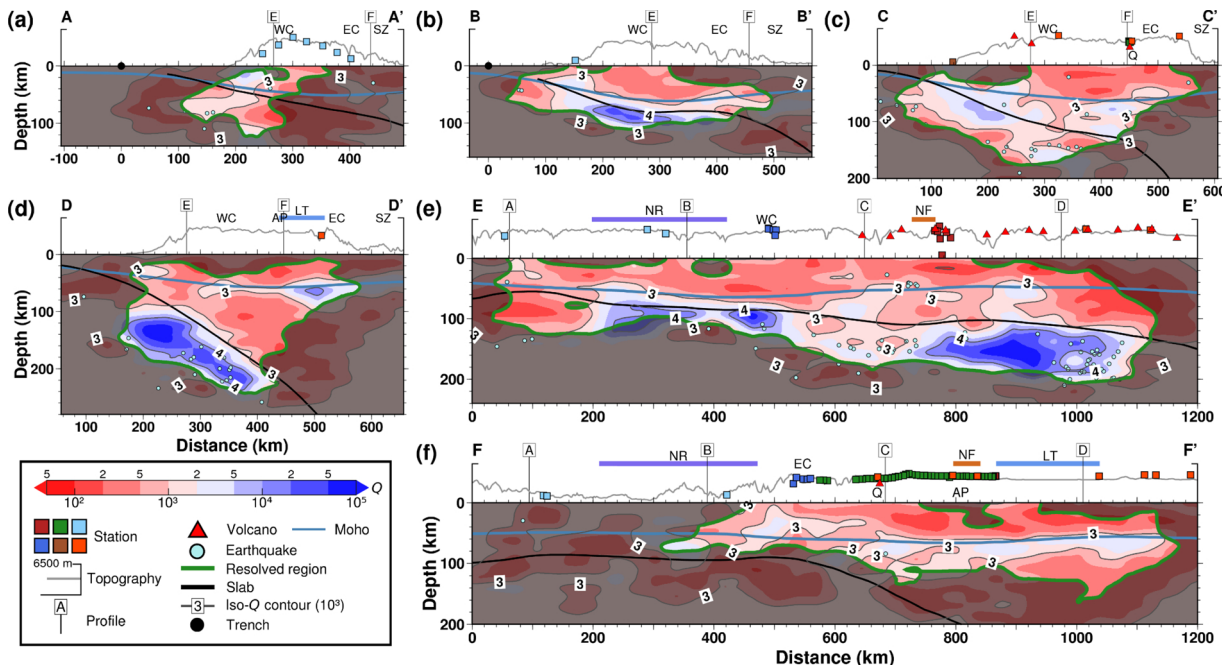


Fig. 8. Q_s in cross-section view along trench-perpendicular profiles (a) A–A', (b) B–B', (c) C–C' and (d) D–D' and trench-parallel profiles (e) E–E' and (f) F–F' for which the locations are indicated in Fig. 1. Lengths of the profiles in (a–d) and (e–f) are 600 km and 1200 km, respectively. The position of 0 km point in the trench-perpendicular profiles (a–d) marks the trench location. Contour level for Q_s is labeled by exponent. The locations for Nazca Ridge (NR), Nazca fracture zone (NF) and Lake Titicaca (LT) are highlighted in the trench-parallel profiles (e and f) (see Fig. S1 for the projected locations of NR and NF). WC—Western Cordillera. EC—Eastern Cordillera. AP—Altiplano Plateau. SZ—Subandean Zone. LT—Lake Titicaca. Q—Quimsachata volcano.

below the volcano (Quimsachata) are shown along the profiles C–C' and F–F' (Figs. 7c, f, 8c, and f). This volcano is located in an isolated area far east of the main volcanic front (Fig. 1).

5.2.3. Mantle layer between the continental crust and the Nazca slab

The mantle layer corresponds to the imaged region between the base of the continental crust (Laske et al., 2013) and the top slab interface defined in Slab 1.0 model (Hayes et al., 2012). The thickness of this mantle layer is increasing as the Nazca slab transitions from nearly horizontal to normal-dip (Figs. 7 and 8). In the region north of the ridge axis, its thickness is quite thin (< 10 km), and thus meaningful interpretation for the forearc mantle wedge can be difficult. However, in the region south of the ridge axis, we can differentiate the mantle wedge into an oceanward high-Q and a landward low-Q regions with respect to the active arc position (Figs. 7c–f and 8c–f). In particular, we obtain high Q_p and Q_s in lower crust and upper part of the mantle wedge below Lake Titicaca (profiles D–D' and F–F'; Figs. 7d, f, 8d, and f).

5.3. Q_p/Q_s structure

The ratio of Q_p and Q_s (Q_p/Q_s) ranges between 0.5 and 1.5 in the Nazca Plate subduction zone (Fig. 9), and on average Q_p/Q_s is close to 1.0. In particular, there are several zones with $Q_p/Q_s > 1.0$, which are lower continental crust, mantle wedge, and upper part of the subducting slab along the profiles C–C' and D–D' (Figs. 9c–f). The zones with $Q_p/Q_s < 0.8$ are mostly located in the forearc crust and mantle wedge (Figs. 9b–f).

6. Discussion

6.1. Subduction-zone structure

6.1.1. High-Q zone for the subducting Nazca plate

The 3D attenuation models in terms of Q_p and Q_s presented here provide the clearest pictures of various structural elements and also

provide constraints on the thermo-petrological environment of the study region. Our Q models overall show well-defined along-arc slab structure down to a depth of 225 km, expressed in terms of the low attenuation anomaly (Figs. 5–8, S4, and S5). Most of the relocated seismicity is confined within the subducting slab, and those overall define the plate interface geometry. In particular, our Q models along the profile nearest to the Nazca ridge axis (profile B–B') show that the Nazca slab subducts at a 30° dipping angle down to 80–85 km depth, and then transitions into a horizontal geometry for ~200 km (at 200–400 km from the trench) along the trench-perpendicular direction (Figs. 7b and 8b). Also, we obtain the highest Q_p and Q_s estimates nearest to the top plate interface of the flat slab (Figs. 7b and 8 b). Although our model domain along the profile B–B' is limited to a distance of ~400 km or ~500 km for Q_s and Q_p , respectively, from the trench, the flat slab extends further inland for approximately 100 km based on receiver functions (Phillips and Clayton, 2014; Ma and Clayton, 2015).

The flat slab, except the region north of the ridge axis, is clearly associated with lower attenuation than those of the slab-dip transition region and the normal-dip slab region (Figs. 7a–e and 8a–e). Such low attenuation along the flat slab is consistent with elevated P-to-S velocity ratio (V_p/V_s) from the teleseismic receiver functions (Kim and Clayton, 2015) and low seismic velocities from the double-difference tomography (Lim et al., 2018). The observed along-arc differences in such seismological properties can be attributed to different hydration states between the flat and normal-dip slabs due to the subduction of the Nazca Ridge (Kim and Clayton, 2015). Similar observation has been made in central Mexico subduction zone, where the Cocos slab transitions from flat to normal-dipping (Kim et al., 2012, 2013).

We observe that the high-Q feature for the dipping slab in the slab-dip transition zone is less clear (Figs. 7c and 8c), while the highest ray coverage is obtained in this region. Farther southeast, normal-dip slab in southern most Peru and northwestern Bolivia is clearly defined with high Q and seismicity (Figs. 7d and 8d).

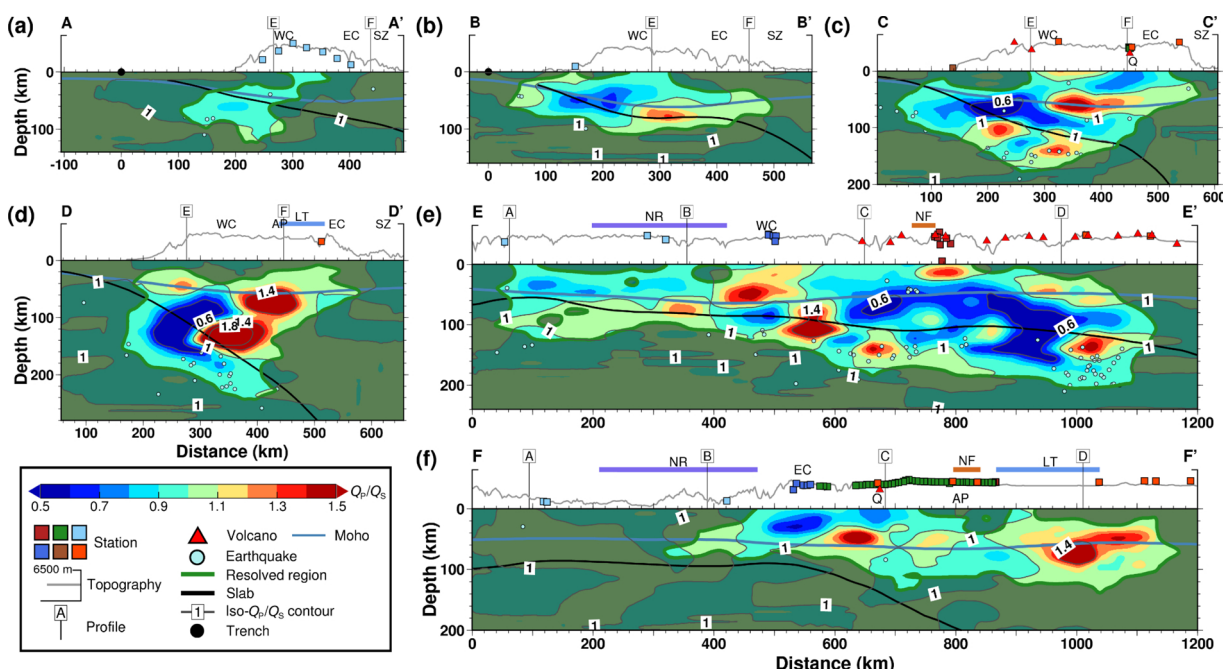


Fig. 9. Q_p/Q_s in cross-section view along trench-perpendicular profiles (a) A–A', (b) B–B', (c) C–C' and (d) D–D' and trench-parallel profiles (e) E–E' and (f) F–F' for which the locations are indicated in Fig. 1. Lengths of the profiles in (a–d) and (e–f) are 600 km and 1200 km, respectively. The position of 0 km point in the trench-perpendicular profiles (a–d) marks the trench location. The locations for Nazca Ridge (NR), Nazca fracture zone (NF) and Lake Titicaca (LT) are highlighted in the trench-parallel profiles (e and f) (see Fig. S1 for the projected locations of NR and NF). WC—Western Cordillera. EC—Eastern Cordillera. AP—Altiplano Plateau. SZ—Subandean Zone. LT—Lake Titicaca. Q—Quimsachata volcano.

6.1.2. Low-Q zone in response to oceanic ridge subduction

We find several localities where higher attenuation is observed at the expected depths for the Nazca slab. The observed high attenuation for the Nazca slab in the north of the ridge axis (extending ~ 200 km along the trench-perpendicular profile A–A'; Figs. 7a and 8a) reflects complex slab structure associated with the southward migrating Nazca Ridge. Offshore seismic data sampling the collision zone of the Nazca Ridge at 15°S show a small sediment input and a high taper of the continental wedge indicating high basal friction, which are characteristics of a margin undergoing intense tectonic erosion (Hampel et al., 2004). Anomalously high attenuation feature in this region may reflect intense tectonic erosion related to the passage of the ridge.

Previous studies discussed low-velocity features in the northwestern region of the ridge axis as a possible slab tear (Antonijevic et al., 2015). Antonijevic et al. (2015) suggested that the flat slab is shallowest along the ridge axis, while to the northwest of the ridge, the slab is torn based on the low-velocity constraints from Rayleigh wave phase velocities. This low-velocity anomaly parallel to the trench is suggested to be the evidence of asthenosphere between the two torn portions of the subducted plate. If this is the case, the low-Q estimates may represent the mantle upwelling associated with the slab tear. The relocated seismicity in the slab-dip transition zone, however, shows no sign of the slab tear (Dougherty and Clayton, 2015; Lim et al., 2018).

The low-Q anomaly is clearly observed in close proximity to current positions of both Nazca and Iquique ridges (Figs. 5a and 6a). Among the various factors contributing to this low Q values, dominant bending-related faults (Hampel et al., 2004) and/or presence of ridge-parallel cracks (Almendros et al., 2000) offshore can induce the reduction in Q values.

6.1.3. Low-Q zone in the mantle wedge

Upon subduction, the fluids released from the subducting slab modify physical and chemical properties of the mantle wedge. In particular, long-term supply of fluid from the southward migrating Nazca Ridge provides additional buoyancy of the subducting oceanic lithosphere and also lowers the viscosity of the overlying mantle wedge to drive and sustain the flat slab geometry (Kim and Clayton, 2015). The presence of a thin mantle wedge is important in Peruvian flat-slab system because the constriction of the mantle layer inhibits typical asthenospheric corner flow, leading to a large negative pressure that further decreases the dip of the slab (Ma and Clayton, 2015). Also, the leading edge of the mantle wedge (i.e. nose) is expected to show little attenuation because of inefficient wedge corner flow (Stachnik et al., 2004).

Previous studies have emphasized the importance of the “cold nose”, where peridotites thrust over subducting sediments and oceanic crust (e.g., Wiens et al., 2008). Reaction of mantle peridotite with the slab-derived fluids drives retrograde metamorphism, forming hydrous minerals such as serpentine and talc (Kelemen and Manning, 2015). Seismic properties such as low seismic velocities (Hyndman and Peacock, 2003) and high attenuation (e.g., Stachnik et al., 2004) in the mantle wedge nose can thus be attributed to retrograde metamorphism. Serpentine and talc in the nose are mechanically weak materials that decouple the forearc crust from the subducting slab. Cooling of the nose is considered to be the cause of low heat flow in forearcs (e.g., Springer and Forster, 1998). In addition, previous numerical study by Wada et al. (2011) reported that sharp transition in Q near the arc, indicating sharp thermal transition in the forearc mantle wedge, depends strongly on the mantle rheology.

In southern Peru, since the mantle layer is quite thin (< 10 km) between the upper and subducting plates in the region north of the ridge axis, it is difficult to confidently observe low attenuation for ~ 100 km from the coast in the forearc mantle wedge (Figs. 7a, b, 8a, and b). Whereas, the low attenuation in the forearc mantle wedge is more obvious in the region south of the ridge axis (Figs. 7c, d, 8c and d), suggesting the presence of cold viscous nose.

The hydration process within the forearc mantle is closely related to serpentization, which can drastically reduce the seismic velocity and density of the mantle while increasing Poisson's ratio (and V_p/V_s) (Hyndman and Peacock, 2003), and thus can affect the seismic attenuation. Previous velocity tomography study by Lim et al. (2018) suggested that generally depressed seismic velocities and elevated V_p/V_s in the forearc mantle indicate an overall low degree of serpentization in the slab-dip transition zone. The low degree of serpentization can be attributed to slow dehydration of the slab because of relatively old age of the oceanic plate (Abers et al., 2017). Based on the seismic velocities from the inversion (Lim et al., 2018), the degree of serpentization in the flat slab, the slab-dip and the normal-dip regions are 10–30%, 0–20% and 5–15%, respectively (Hyndman and Peacock, 2003). Relatively higher degree of mantle serpentization in the flat slab region than that in the other regions can be attributed to hydrous compositions in the subducting ridge (Kim and Clayton, 2015). Due to relatively low degree of serpentization, sharp transition in Q, thus thermal state, in the forearc mantle wedge is expected (Wada et al., 2011), and we also observe such feature in the profiles crossing the normal-dip slab region (Figs. 7c, d, 8c and d).

More prominent low-Q zones are observed in the mantle wedge beneath the volcanic arc front and backarc regions (Figs. 7c, e, 8c, and e), which reflect the source zones of arc magmatism due to slab dehydration. Q_p/Q_s variations (together with V_p/V_s from Lim et al. (2018)) can provide useful relationships between attenuation and rock properties in the mantle wedge. If Q_p and Q_s distributions are drastically different in places, this may provide proxy for different process reflecting the contribution of scattering, absorption, or temperature to Q. We obtain relatively high Q_p/Q_s of 1.0–1.5 in the backarc mantle wedge in the normal slab-dip zone and high Q_p/Q_s (~ 1.5) below Lake Titicaca (Figs. 9d and f, respectively). The observed location for the high Q_p/Q_s (Fig. 9f) is coincident with the high Q_p and Q_s for the Brazilian Shield underplating from the west (Figs. 7d and 8d).

6.2. Upper-plate attenuation structure

Seismic velocity and attenuation anomalies at the mantle depth are commonly interpreted in terms of temperature variations on the basis of laboratory studies of elastic and anelastic properties of rocks (Artemieva et al., 2004). Furthermore, strong correlation between Q_s and V_s in the upper mantle has been observed in many regions of active tectonics (e.g., Tsumura et al., 2000). However, in regions of active tectonics (e.g., South America subduction zone), temperature effects alone cannot explain Q_s and V_s in the continental lithosphere. It is likely that partial melts and/or fluids may affect seismic parameters in these regions. Artemieva et al. (2004) demonstrated that lithospheric temperature plays the dominant role in controlling Q_s and V_s anomalies, but other physical parameters, such as compositional variations, fluids, partial melting and scattering, may also play a key role in determining Q_s and V_s variations in the continental mantle.

6.2.1. Western Cordillera

The locations for the high-attenuation anomalies at crustal depths (Figs. 5a, b, 6a, and b) are well correlated with the active volcanic arc front situated in the Western Cordillera. We also observe high attenuation below Quimsachata, the active volcano in an isolated area far east of the main volcanic front (Figs. 5a, b, 6a, and b).

6.2.2. Altiplano Plateau and Eastern Cordillera

Moderately high attenuation in the upper plate in the southern part of our study region can be linked to tectonic structures such as the Altiplano Plateau and Eastern Cordillera. The Eastern Cordillera is an inactive fold and thrust belt that contains Triassic and Miocene plutons (Garzzone et al., 2017 and references therein). Previously low-velocity zone was identified by Dorbath et al. (1993) in the same localities where we observe low Q (Figs. 5a, b, 6a, and b), and suggested due to

mantle upwelling. Numerous studies for the region in Chile and Bolivia reported low velocity features below the Eastern Cordillera (Myers et al., 1998; Beck and Zandt, 2002; Elger et al., 2005; Asch et al., 2006; Schurr et al., 2006; Heit et al., 2007; Kay and Coira, 2009). We note that the poor correlation between Q and V_s is found beneath Altiplano where the deepest Moho (75 km, maximum) is expected (Phillips et al., 2012), when our Q models sliced at 75 km depth (Figs. 5b and 6b) are compared with the V_s model at 80 km depth by Ward et al. (2016). Our low Q features at 75 km depth extend further down to the upper mantle of the continental lithosphere, supporting the presence of mantle upwelling in this region. Together with the presence of Brazilian Shield at this depth range, factors such as compositional/structural variations, fluids, partial melting, and scattering can contribute to the weak correlation between Q and V_s within the continental lithosphere beneath Altiplano Plateau and Eastern Cordillera.

6.2.3. Brazilian Shield

Prominent high- Q_p zone in depth range of ~ 40 – 80 km is present in the southernmost profile D–D' (~ 600 km away from the trench) beneath Eastern Cordillera and Subandean Zone (Fig. 7d). Along the same profile, we find a similar structure from Q_s (Fig. 8d), but its resolution is slightly poor due to less S ray coverage. The degree of attenuation diminishes northwest, and we do not observe the feature at the southern end of the flat-slab region in profile B–B' (Figs. 7b and 8b). Our observed high- Q_p zone corresponds to the region that shows high velocities in both the crust and upper mantle under the Subandean Zone (Phillips et al., 2012; Scire et al., 2016). In particular, upper-most part of the observed low-attenuation feature agrees well with the receiver function images from PE and PF stations (Fig. 1) suggesting the upper part of the underthrusting Brazilian Shield (Phillips et al., 2012; Phillips and Clayton, 2014). Strong teleseismic converted amplitudes at ~ 40 km and crustal seismicity beneath the Eastern Cordillera and Subandean zone define the top interface of the Brazilian Shield as a thrust fault (Ma and Clayton, 2015).

Although the timing and cause of the Central Andes Plateau is debated (Garzione et al., 2017 and references therein), if above-mentioned seismic properties at the depth for lower crust and uppermost mantle are linked with the underthrusting cratonic lithosphere, the underthrusted craton can contribute to the crustal thickening observed beneath the Altiplano (Moho depth of 70–75 km beneath the Altiplano; Phillips et al., 2012). This tectonic model supports a gradual uplift of the plateau due to thickening and shortening of the crust (Elger et al., 2005; McQuarrie et al., 2005; Oncken et al., 2006) rather than a rapid uplift since 10 Ma (Garzione et al., 2008) resulting from large-scale delamination of lithosphere (Schurr et al., 2006). The western limit of the underthrusted feature extends to the Eastern Cordillera, and it does not appear to extend beyond the volcanic arc in the Western Cordillera (Figs. 7d and 8d).

6.3. Inferred thermal structure

As the angle of the subduction changes along strike, the subducting plate is forced to bend and deform to accommodate the change in the subduction angle. Our Q model as well as previous seismic studies shows significant along-arc variability in both subducting slab and mantle layer above the slab, corresponding to the rapid change in slab geometry. The geometry of the subducting slab is expected to affect mantle flow. In particular, previous shear-wave splitting measurements (Eakin and Long, 2013; Eakin et al., 2014, 2015; Eakin et al., 2016) showed a sharp transition in the splitting pattern with respect to the Nazca ridge axis, suggesting that the ridge indeed plays an important role in subduction-zone dynamics and mantle flow in the flat-slab system. As discussed earlier, since the mantle layer is quite thin in the flat-slab system, the constriction of the mantle layer between the flat slab and the thick continental crust inhibits typical asthenospheric corner flow, leading to a large negative pressure that further decreases

the dip angle of the slab (Ma and Clayton, 2015). The presence of a thick (Ryan et al., 2016; Bishop et al., 2017) and cold continental lithosphere (Currie and Hyndman, 2006) may also act as a partial barrier to the mantle-wedge flow, resulting in a decreased pressure in the mantle-wedge corner (O'Driscoll et al., 2012).

The decreasing dip of the slab also indicates a decreasing influx of asthenospheric mantle above the slab. As a result, the slab flattening process significantly cools the system, particularly the upper lithosphere (e.g., Ramos et al., 2002), and a decreasing degree of partial mantle melting is expected at the arc location eventually shutting off arc magmatism in the flat slab region. Our relatively high Q in the forearc mantle wedge and low Q in backarc region (crust and mantle) support the geological evidence listed above.

7. Conclusions

Subduction-zone seismic attenuation for the Nazca subduction zone is a key parameter that can reveal complex geodynamic processes caused by interaction of subducting Nazca slab and Nazca Ridge with the surrounding mantle and/or continental plate. The dense seismic array data collected in southern Peru and northwestern Bolivia can provide further constraints on the nature of the along-strike and along-dip transition in seismic attenuation in terms of a quality factor Q . The checkerboard test results ensure the highest resolution in the region where the slab geometry changes from nearly horizontal to normal-dip, at the depth range of ~ 30 – 150 km including the continental crust, mantle wedge and subducting slab. In this study, we provide the first seismic attenuation models (Q_p , Q_s , and Q_p/Q_s structures) based on the regional earthquakes. We obtain five main features in our attenuation model including (1) well-defined along-strike and along-dip Nazca slab structure in terms of low attenuation ($Q_p = 5 \times 10^2$ – 1×10^5 ; $Q_s = 5 \times 10^2$ – 1×10^5), (2) high attenuation in regard to the oceanic ridge subduction north of the Nazca Ridge axis ($Q_p = 1 \times 10^2$ – 1×10^3 ; $Q_s = 1 \times 10^2$ – 1×10^3), reflecting complex nature of the subducting slab, (3) high attenuation in the mantle wedge ($Q_p = 5 \times 10^1$ – 1×10^3 ; $Q_s = 5 \times 10^1$ – 5×10^3) and continental crust ($Q_p = 5 \times 10^1$ – 1×10^3 ; $Q_s = 5 \times 10^1$ – 1×10^3), (4) clear low attenuation feature for underthrusting Brazilian Shield below Eastern Cordillera and Subandean Zone, and (5) high attenuation related to the slab dehydration beneath the volcanic arc at 100 and 200 km depths ($Q_p = 5 \times 10^2$ – 1×10^3 ; $Q_s = 2 \times 10^2$ – 1×10^3). In particular, prominent low- Q zones in the continental crust and mantle wedge beneath the active volcanic arc reflect source zones of arc magmatism caused by fluids from the slab dehydration. Although the cold mantle wedge nose is less clear in the flat-slab system because of spatial resolution, high- Q is well observed in the forearc mantle in the southern region, reflecting its cold and viscous nature, which greatly affects the upper-plate structure of southern Peru.

Acknowledgement

H. Jang, Y. Kim, and H. Lim acknowledge Creative-Pioneering Researchers Program through Seoul National University (SNU SRnD 3345-20160014), and the Nuclear Safety Research Program through the Korea Foundation of Nuclear Safety (KoFONS), granted financial resource from the Nuclear Safety and Security Commission (NSSC), Republic of Korea (No. 1705010). The authors are grateful to the many institutions that deployed and maintained temporary networks in southern Peru and northwestern Bolivia. In particular, the authors thank the Peru Subduction Experiment (PeruSE) for providing the seismic waveform data used in this study. Seismic instruments for the Central Andean Uplift and Geodynamics of High Topography (CAUGHT) and the Peru Lithosphere and Slab Experiment (PULSE) experiments were provided by the Incorporated Research Institutions for Seismology (IRIS) through the Program for the Array Seismic Studies of the Continental Lithosphere (PASSCAL) Instrument Center at

the New Mexico Institute of Mining and Technology. Finally, the authors thank Editor Kelin Wang and the two reviewers for their comments, which greatly improved this article.

Appendix A. Supplementary data

Supplementary material related to this article can be found, in the online version, at <https://doi.org/10.1016/j.tecto.2019.228203>.

References

- Abers, G.A., Sarker, G., 1996. Dispersion of regional body waves at 100–150 km depth beneath Alaska: in situ constraints on metamorphism of subducted crust. *Geophys. Res. Lett.* 23, 1171–1174. <https://doi.org/10.1029/96GL00974>.
- Abers, G.A., van Keken, P.E., Hacker, B.R., 2017. The cold and relatively dry nature of mantle forearcs in subduction zones. *Nat. Geosci.* 10, 333–337. <https://doi.org/10.1038/ngeo2922>.
- Aizawa, Y., Barnhoorn, A., Faul, U.H., Fitz Gerald, J.D., Jackson, I., Kovács, I., 2008. Seismic properties of Anita Bay dunite: an exploratory study of the influence of water. *J. Petrol.* 49, 841–855. <https://doi.org/10.1093/petrology/egn007>.
- Allmendinger, R.W., Jordan, T.E., Kay, S.M., Isacks, B.L., 1997. The evolution of the altiplano-puna plateau of the central andes. *Annu. Rev. Earth Planet. Sci.* 25, 139–174. <https://doi.org/10.1146/annurev.earth.25.1.139>.
- Almendros, J., Barclay, A.H., Wilcock, W.S.D., Purdy, G.M., 2000. Seismic anisotropy of the shallow crust at the Juan de Fuca Ridge. *Geophys. Res. Lett.* 27, 3109–3112. <https://doi.org/10.1029/2000GL011535>.
- Amante, C., Eakins, B.W., 2009. ETOPO1 1 Arc-Minute Global Relief Model: Procedures, Data Sources and Analysis. NOAA Technical Memorandum NESDIS NGDC-24. National Geophysical Data Center. NOAA. <https://doi.org/10.7289/V5C8276M>.
- Anderson, J.G., Hough, S.E., 1984. A model for the shape of the fourier amplitude spectrum of acceleration at high frequencies. *Bull. Seismol. Soc. Am.* 74, 1969–1993.
- Antonijevic, S.K., Wagner, L., Kumar, A., Beck, S.L., Long, M.D., Zandt, G., Tavera, H., Condori, C., 2015. The role of ridges in the formation and longevity of flat slabs. *Nature* 524, 212–215. <https://doi.org/10.1038/nature14648>.
- Artemieva, I.M., Billien, M., Leveque, J.-J., Mooney, W.D., 2004. Shear wave velocity, seismic attenuation, and thermal structure of the continental upper mantle. *Geophys. J. Int.* 157, 607–628. <https://doi.org/10.1111/j.1365-246X.2004.02195.x>.
- Asch, G., Schurr, B., Bohm, M., Yuan, X., Haberland, C., Heit, B., Kind, R., Woelbern, I., Bataille, K., Comte, D., Pardo, M., Viramont, J., Rietbrock, A., Giese, P., 2006. Seismological studies of the central and southern Andes. The Andes. Springer, Berlin Heidelberg, pp. 443–457. https://doi.org/10.1007/978-3-540-48684-8_21.
- Beck, S.L., Zandt, G., 2002. The nature of orogenic crust in the central Andes. *J. Geophys. Res. Solid Earth* 107. <https://doi.org/10.1029/2000jb000124>.
- ESE 7-1–ESE 7-16.
- Beck, S., Zandt, G., Wagner, L., 2010. Central Andean uplift and the geodynamics of the high topography. International Federation of Digital Seismography Networks. https://doi.org/10.7914/SN/ZG_2010. Dataset/Seismic Network.
- Bevis, M., Kendrick, E., Smalley, R., Brooks, B., Allmendinger, R., Isacks, B., 2001. On the strength of interplate coupling and the rate of back arc convergence in the central Andes: an analysis of the interseismic velocity field. *Geochem. Geophys. Geosyst.* 2, <https://doi.org/10.1029/2001GC000198>.
- Bishop, B.T., Beck, S.L., Zandt, G., Wagner, L., Long, M., Antonijevic, S.K., Kumar, A., Tavera, H., 2017. Causes and consequences of flat-slab subduction in southern Peru. *Geosphere* 13, 1392–1407. <https://doi.org/10.1130/GES01440.1>.
- Brune, J.N., 1970. Tectonic stress and the spectra of seismic shear waves from earthquakes. *J. Geophys. Res.* 75, 4997–5009. <https://doi.org/10.1029/JB075i026p04997>.
- Cahill, T., Isacks, B.L., 1992. Seismicity and shape of the subducted Nazca Plate. *J. Geophys. Res.* 97, 17503. <https://doi.org/10.1029/92JB00493>.
- Chen, T., Clayton, R.W., 2009. Seismic attenuation structure in central Mexico: image of a focused high-attenuation zone in the mantle wedge. *J. Geophys. Res. Solid Earth* 114, 1–9. <https://doi.org/10.1029/2008JB005964>.
- Currie, C.A., Hyndman, R.D., 2006. The thermal structure of subduction zone back arcs. *J. Geophys. Res.* 111, B08404. <https://doi.org/10.1029/2005JB004024>.
- Dorbath, C., Granet, M., Poupinet, G., Martinez, C., 1993. A teleseismic study of the Altiplano and the eastern Cordillera in northern Bolivia: new constraints on a lithospheric model. *J. Geophys. Res.* 98, 9825. <https://doi.org/10.1029/92JB02406>.
- Dougherty, S.L., Clayton, R.W., 2015. Seismic structure in southern Peru: evidence for a smooth contortion between flat and normal subduction of the Nazca Plate. *Geophys. J. Int.* 200, 534–555. <https://doi.org/10.1093/gji/ggu415>.
- Eakin, C.M., Long, M.D., 2013. Complex anisotropy beneath the Peruvian flat slab from frequency-dependent, multiple-phase shear wave splitting analysis. *J. Geophys. Res. Solid Earth* 118, 4794–4813. <https://doi.org/10.1002/jgrb.50349>.
- Eakin, C.M., Long, M.D., Beck, S.L., Wagner, L.S., Tavera, H., Condori, C., 2014. Response of the mantle to flat slab evolution: insights from local S splitting beneath Peru. *Geophys. Res. Lett.* 41, 3438–3446.
- Eakin, C.M., Long, M.D., Wagner, L.S., Beck, S.L., Tavera, H., 2015. Upper mantle anisotropy beneath Peru from SKS splitting: constraints on flat slab dynamics and interaction with the Nazca Ridge. *Earth Planet. Sci. Lett.* 412, 152–162. <https://doi.org/10.1016/j.epsl.2014.12.015>.
- Eakin, C.M., Long, M.D., Scire, A., Beck, S.L., Wagner, L.S., Zandt, G., Tavera, H., 2016. Internal deformation of the subducted Nazca slab inferred from seismic anisotropy. *Nat. Geosci.* 9, 56–59. <https://doi.org/10.1038/ngeo2592>.
- Eberhart-Phillips, D., Chadwick, M., 2002. Three-dimensional attenuation model of the shallow Hikurangi subduction zone in the Raukumara Peninsula, New Zealand. *J. Geophys. Res.* 107. <https://doi.org/10.1029/2000jb000046>.
- Elger, K., Oncken, O., Glodny, J., 2005. Plateau-style accumulation of deformation: southern Altiplano. *Tectonics* 24. <https://doi.org/10.1029/2004TC001675>.
- Faul, U.H., Fitz Gerald, J.D., Jackson, I., 2004. Shear wave attenuation and dispersion in melt-bearing olivine polycrystals: 2. Microstructural interpretation and seismological implications. *J. Geophys. Res. Solid Earth* 109. <https://doi.org/10.1029/2003JB002407>.
- Garzione, C.N., Hoke, G.D., Libarkin, J.C., Withers, S., MacFadden, B., Eiler, J., Ghosh, P., Mulch, A., 2008. Rise of the Andes. *Science* 320, 1304–1307. <https://doi.org/10.1126/science.1148615>.
- Garzione, C.N., McQuarrie, N., Perez, N.D., Ehlers, T.A., Beck, S.L., Kar, N., Eichelberger, N., Chapman, A.D., Ward, K.M., Ducea, M.N., Lease, R.O., Poulsen, C.J., Wagner, L.S., Saylor, J.E., Zandt, G., Horton, B.K., 2017. Tectonic evolution of the Central Andean Plateau and implications for the growth of plateaus. *Annu. Rev. Earth Planet. Sci.* 45, 529–559. <https://doi.org/10.1146/annurev-earth-063016-020612>.
- Garth, T., Rietbrock, A., 2017. Constraining the hydration of the subducting Nazca plate beneath northern Chile using subduction zone guided waves. *Earth Planet. Sci. Lett.* 474, 237–247. <https://doi.org/10.1016/j.epsl.2017.06.041>.
- GTSN, 1993. Global telemetered seismograph network. Albuquerque Seismological Laboratory and US Geological Survey. Dataset. <https://doi.org/10.7914/SN/GT>.
- Gutscher, M.A., Spakman, W., Bijwaard, H., Engdahl, E.R., 2000. Geodynamics of flat subduction: seismicity and tomographic constraints from the Andean margin. *Tectonics* 19, 814–833. <https://doi.org/10.1029/1999TC001152>.
- Haberland, C., Rietbrock, A., 2004. Attenuation tomography in the western central Andes: a detailed insight into the structure of a magmatic arc. *J. Geophys. Res. Solid Earth* 106, 11151–11167. <https://doi.org/10.1029/2000jb900472>.
- Hampel, A., 2002. The migration history of the Nazca Ridge along the Peruvian active margin: a re-evaluation. *Earth Planet. Sci. Lett.* 203, 665–679. [https://doi.org/10.1016/S0012-821X\(02\)00859-2](https://doi.org/10.1016/S0012-821X(02)00859-2).
- Hampel, A., Adam, J., Kukowski, N., 2004. Response of the tectonically erosive south Peruvian forearc to subduction of the Nazca Ridge: analysis of three-dimensional analogue experiments. *Tectonics* 23. <https://doi.org/10.1029/2003TC001585>.
- Hansen, P.C., 2000. The L-curve and its use in the numerical treatment of inverse problem. *Computational Inverse Problems in Electrocardiology*. WIT Press.
- Hayes, G.P., Wald, D.J., Johnson, R.L., 2012. Slab1.0: a three-dimensional model of global subduction zone geometries. *J. Geophys. Res. Solid Earth* 117. <https://doi.org/10.1029/2011JB008524>.
- Heit, B., Sodoudi, F., Yuan, X., Bianchi, M., Kind, R., 2007. An S receiver function analysis of the lithospheric structure in South America. *Geophys. Res. Lett.* 34, L14307. <https://doi.org/10.1029/2007GL030317>.
- Hu, J., Liu, L., 2016. Abnormal seismological and magmatic processes controlled by the tearing South American flat slabs. *Earth Planet. Sci. Lett.* 450, 40–51. <https://doi.org/10.1016/j.epsl.2016.06.019>.
- Hyndman, R.D., Peacock, S.M., 2003. Serpentization of the forearc mantle. *Earth Planet. Sci. Lett.* 212, 417–432. [https://doi.org/10.1016/S0012-821X\(03\)00263-2](https://doi.org/10.1016/S0012-821X(03)00263-2).
- Kanamori, H., Anderson, D.L., 1975. Theoretical basis of some empirical relations in seismology. *Bull. Seismol. Soc. Am.* 65, 1073–1095.
- Kang, H., Kim, Y., 2019. Localized anisotropic subduction-zone structure in southern Peru: constraints from teleseismic receiver functions and forward modeling. *Seismol. Res. Lett.* 90, 1820–1835. <https://doi.org/10.1785/0220180384>.
- Kanzow, C., Yamashita, N., Fukushima, M., 2004. Levenberg–Marquardt methods with strong local convergence properties for solving nonlinear equations with convex constraints. *J. Comput. Appl. Math.* 172, 375–397.
- Kay, S.M., Coira, B.L., 2009. Shallowing and steepening subduction zones, continental lithospheric loss, magmatism, and crustal flow under the Central Andean Altiplano-Puna Plateau, in: backbone of the Americas: shallow Subduction, Plateau Uplift, and Ridge and Terrane Collision. Geological Society of America 229–259. [https://doi.org/10.1130/2009.2014\(11\)](https://doi.org/10.1130/2009.2014(11)).
- Kelemen, P.B., Manning, C.E., 2015. Reevaluating carbon fluxes in subduction zones, what goes down, mostly comes up. *Proc. Natl. Acad. Sci. U.S.A.* 112, 30. <https://doi.org/10.1073/pnas.1507889112>.
- Kim, Y., Clayton, R.W., Jackson, J.M., 2010. Geometry and seismic properties of the subducting Cocos plate in central Mexico. *J. Geophys. Res.* 115, B06310. <https://doi.org/10.1029/2009JB006942>.
- Kim, Y., Clayton, R.W., Jackson, J.M., 2012. Distribution of hydrous minerals in the subduction system beneath Mexico. *Earth Planet. Sci. Lett.* 341–344, 58–67. <https://doi.org/10.1016/j.epsl.2012.06.001>.
- Kim, Y., Clayton, R.W., Asimow, P.D., Jackson, J.M., 2013. Generation of talc in the mantle wedge and its role in subduction dynamics in central Mexico. *Earth Planet. Sci. Lett.* 384, 81–87. <https://doi.org/10.1016/j.epsl.2013.10.006>.
- Kim, Y., Clayton, R.W., 2015. Seismic properties of the Nazca oceanic crust in southern Peruvian subduction system. *Earth Planet. Sci. Lett.* 429, 110–121. <https://doi.org/10.1016/j.epsl.2015.07.055>.
- Ko, Y.T., Kuo, B.Y., Hung, S.H., 2012. Robust determination of earthquake source parameters and mantle attenuation. *J. Geophys. Res. Solid Earth* 117, 1–17. <https://doi.org/10.1029/2011JB008759>.
- Lahr, J.C., 1989. HYPOELLISE: a computer program for determining local earthquake hypocentral parameters, magnitude, and first motion pattern. USGS. <https://doi.org/10.3133/ofr89116>.
- Laske, G., Masters, G., Ma, Z., Pasquenos, M., 2013. Update on crust1.0-a 1-degree global model of earth's crust. *Geophysical Research Abstracts EGU General Assembly*.
- Lim, H., Kim, Y., Clayton, R.W., Thurber, C.H., 2018. Seismicity and structure of Nazca Plate subduction zone in southern Peru. *Earth Planet. Sci. Lett.* 498, 334–347. <https://doi.org/10.1016/j.epsl.2018.07.014>.

- Ma, Y., Clayton, R.W., 2015. Flat slab deformation caused by interplate suction force. *Geophys. Res. Lett.* 42, 7064–7072. <https://doi.org/10.1002/2015GL065195>.
- Martin, S., Rietbrock, A., 2006. Guided waves at subduction zones: dependencies on slab geometry, receiver locations and earthquake sources. *Geophys. J. Int.* 167, 693–704. <https://doi.org/10.1111/j.1365-246X.2006.02963.x>.
- Matthews, K.J., Müller, R.D., Wessel, P., Whitaker, J.M., 2011. The tectonic fabric of the ocean basins. *J. Geophys. Res.* 116, B12109. <https://doi.org/10.1029/2011JB008413>.
- McQuarrie, N., Horton, B.K., Zandt, G., Beck, S., DeCelles, P.G., 2005. Lithospheric evolution of the Andean fold-thrust belt, Bolivia, and the origin of the central Andean plateau. *Tectonophysics* 399, 15–37. <https://doi.org/10.1016/j.tecto.2004.12.013>.
- Myers, S.C., Beck, S., Zandt, G., Wallace, T., 1998. Lithospheric-scale structure across the Bolivian Andes from tomographic images of velocity and attenuation for P and S waves. *J. Geophys. Res. Solid Earth* 103, 21233–21252. <https://doi.org/10.1029/98JB00956>.
- Norabuena, E., Leffler-Griffin, L., Mao, A., Dixon, T., Stein, S., Sacks, I.S., Ocola, L., Ellis, M., 1998. Space geodetic observations of nazca-south america convergence across the central andes. *Science* 279, 358–362. <https://doi.org/10.1126/science.279.5349.358>.
- O'Driscoll, L.J., Richards, M.A., Humphreys, E.D., 2012. Nazca-South America interactions and the late Eocene-late Oligocene flat-slab episode in the central Andes. *Tectonics* 31. <https://doi.org/10.1029/2011TC003036>.
- Oncen, O., Chong, G., Franz, G., Giese, P., Götz, H.-J., Ramos, V.A., Strecker, M.R., Wigger, P., 2006. The Andes: active subduction orogeny. Springer-Verlag, Frontiers in Earth Sciences. Springer, Berlin. <https://doi.org/10.1007/978-3-540-48684-8>.
- PeruSE, 2013. Caltech. Dataset. Peru subduction experiment. <https://doi.org/10.7909/C3H41PBZ>.
- Phillips, K., Clayton, R.W., Davis, P., Tavera, H., Guy, R., Skinner, S., Stubailo, I., Audin, L., Aguilar, V., 2012. Structure of the subduction system in southern Peru from seismic array data. *J. Geophys. Res. Solid Earth* 117. <https://doi.org/10.1029/2012JB009540>.
- Phillips, K., Clayton, R.W., 2014. Structure of the subduction transition region from seismic array data in southern Peru. *Geophys. J. Int.* 196, 1889–1905. <https://doi.org/10.1093/gji/gjt504>.
- Porter, R., Gilbert, H., Zandt, G., Beck, S., Warren, L., Calkins, J., Alvarado, P., Anderson, M., 2012. Shear wave velocities in the Pampean flat-slab region from Rayleigh wave tomography: implications for slab and upper mantle hydration. *J. Geophys. Res.* 117, B11301. <https://doi.org/10.1029/2012JB009350>.
- Prieto, G.A., Parker, R.L., Vernon, F.L., 2009. A Fortran 90 library for multitaper spectrum analysis. *Comput. Geosci.* 35, 1701–1710. <https://doi.org/10.1016/j.cageo.2008.06.007>.
- Ramos, V.A., Cristallini, E.O., Pérez, D.J., 2002. The Pampean flat-slab of the central Andes. *J. South Am. Earth Sci.* 15, 59–78. [https://doi.org/10.1016/S0895-9811\(02\)00006-8](https://doi.org/10.1016/S0895-9811(02)00006-8).
- Ramos, V.A., Folguera, A., 2009. Andean flat-slab subduction through time. *Geol. Soc. London, Spec. Publ.* 327, 31–54. <https://doi.org/10.1144/SP327.3>.
- Ryan, J., Beck, S., Zandt, G., Wagner, L., Minaya, E., Tavera, H., 2016. Central Andean crustal structure from receiver function analysis. *Tectonophysics* 682, 120–133. <https://doi.org/10.1016/j.tecto.2016.04.048>.
- Rychert, C.A., Fischer, K.M., Abers, G.A., Plank, T., Syracuse, E., Protti, J.M., Gonzalez, V., Strauch, W., 2008. Strong along-arc variations in attenuation in the mantle wedge beneath Costa Rica and Nicaragua. *Geochem. Geophys. Geosyst.* 9. <https://doi.org/10.1029/2008GC002040>.
- Schurr, B., Rietbrock, A., Asch, G., Kind, R., Oncken, O., 2006. Evidence for lithospheric detachment in the central Andes from local earthquake tomography. *Tectonophysics* 415, 203–223. <https://doi.org/10.1016/j.tecto.2005.12.007>.
- Scire, A., Zandt, G., Beck, S., Long, M., Wagner, L., Minaya, E., Tavera, H., 2016. Imaging the transition from flat to normal subduction: variations in the structure of the Nazca slab and upper mantle under southern Peru and northwestern Bolivia. *Geophys. J. Int.* 204, 457–479. <https://doi.org/10.1093/gji/ggv452>.
- Skinner, S.M., Clayton, R.W., 2013. The lack of correlation between flat slabs and bathymetric impactors in South America. *Earth Planet. Sci. Lett.* 371–372, 1–5. <https://doi.org/10.1016/j.epsl.2013.04.013>.
- Springer, M., Forster, A., 1998. Heat-flow density across the central Andean subduction zone. *Tectonophysics* 291, 123–139.
- Stachnik, J.C., Abers, G.A., Christensen, D.H., 2004. Seismic attenuation and mantle wedge temperatures in the Alaska subduction zone. *J. Geophys. Res. Solid Earth* 109, 1–17. <https://doi.org/10.1029/2004JB003018>.
- Tsumura, N., Matsumoto, S., Horiuchi, S., Hasegawa, A., 2000. Three-dimensional attenuation structure beneath the northeastern Japan arc estimated from spectra of small earthquakes. *Tectonophysics* 319, 241–260.
- Um, J., Thurber, C., 1987. A fast algorithm for two-point seismic ray tracing. *Bull. Seismol. Soc. Am.* 77, 972–986.
- Wada, I., Rychert, C.A., Wang, K., 2011. Sharp thermal transition in the forearc mantle wedge as a consequence of nonlinear mantle wedge flow. *Geophys. Res. Lett.* 38, L13308. <https://doi.org/10.1029/2011GL047705>.
- Wagner, L., Beck, S., Long, M., 2010. PerU Lithosphere and Slab Experiment. International Federation of Digital Seismography Networks. https://doi.org/10.7914/SN/ZD_2010.
- Ward, K.M., Zandt, G., Beck, S.L., Wagner, L.S., Tavera, H., 2016. Lithospheric structure beneath the northern central Andean Plateau from the joint inversion of ambient noise and earthquake-generated surface waves. *J. Geophys. Res. Solid Earth* 121, 8217–8238. <https://doi.org/10.1002/2016JB013237>.
- Wiens, D.A., Conder, J.A., Faul, U.H., 2008. The seismic structure and dynamics of the mantle wedge. *Annu. Rev. Earth Planet. Sci.* 34, 421–455. <https://doi.org/10.1146/annurev.earth.33.092203.122633>.
- Zhao, D., Hasegawa, A., Horiuchi, S., 1992. Tomographic imaging of P and S wave velocity structure. *J. Geophys. Res.* 97, 19909–19928. <https://doi.org/10.1029/92JB00603>.